Quantitative Guidelines for Force Calibration through Spectral Analysis of Magnetic Tweezers Data

Aartjan J. W. te Velthuis,[†‡△] Jacob W. J. Kerssemakers,[†△] Jan Lipfert,[†] and Nynke H. Dekker[†*]
[†]Department of Bionanoscience, Kavli Institute of Nanoscience, Delft University of Technology, Delft, The Netherlands; and [‡]Department of Medical Microbiology, Molecular Virology Laboratory, Leiden University Medical Center, Leiden, The Netherlands

ABSTRACT Single-molecule techniques are powerful tools that can be used to study the kinetics and mechanics of a variety of enzymes and their complexes. Force spectroscopy, for example, can be used to control the force applied to a single molecule and thereby facilitate the investigation of real-time nucleic acid-protein interactions. In magnetic tweezers, which offer straightforward control and compatibility with fluorescence measurements or parallel tracking modes, force-measurement typically relies on the analysis of positional fluctuations through video microscopy. Significant errors in force estimates, however, may arise from incorrect spectral analysis of the Brownian motion in the magnetic tweezers. Here we investigated physical and analytical optimization procedures that can be used to improve the range over which forces can be reliably measured. To systematically probe the limitations of magnetic tweezers spectral analysis, we have developed a magnetic tweezers simulator, whose outcome was validated with experimental data. Using this simulator, we evaluate methods to correctly perform force experiments and provide guidelines for correct force calibration under configurations that can be encountered in typical magnetic tweezers experiments.

INTRODUCTION

Recently, single-molecule techniques such as atomic force microscopy, tethered-particle microscopy, optical tweezers, and magnetic tweezers (MTs) have become more and more frequently applied to further our understanding of biological processes. For example, they have become invaluable tools for studies of nucleic acid replication and repair, and have provided information on details of enzyme kinetics such as translocation times, step sizes, and coupling in the mechano-chemical reaction cycle. In addition, they have revealed mechanical properties of both nucleic acid polymers, and provided insight into processes such as recombination (1–5).

Compared to other single-molecule techniques that allow manipulation of externally applied forces, MTs are particularly suited for experiments that cover a force range from femto- up to tens of picoNewtons (6,7), need operation at a constant force, or require parallel measurements when enzyme processivity is limited (8). Moreover, MT setups are relatively straightforward to construct, and consist primarily of an inverted microscope, a set of magnets, and a flow cell. In this flow cell, superparamagnetic beads are physically tethered to a surface via a nucleic acid or protein tether (Fig. 1 *A*) (3,7,9,10), while the magnets positioned above the flow cell create an external, controllable magnetic field. The gradient of this field supplies a force in the z direction (Fig. 1), whereas rotation of the magnetic field applies torque to the tether and introduces supercoils (3,11,12). The ability to apply both force and torque facilitates experiments aimed at studying the different structural forms of nucleic acids (3,13,14). Additionally, this dual mode of manipulation has provided insight into the force- and torque-dependent properties of, e.g., topoisomerases and chromatin (5,15–18).

In the MT, the motions of the bead take place round an equilibrium position due to Brownian motion, and are constrained by both the applied force and the flexibility of the nucleic acid tether (Fig. 1 *B*) (3). The applied force can be computed from the field configuration and the magnetization of the beads according to

$$\vec{F} = \frac{1}{2}\vec{\nabla}(\vec{m}\cdot\vec{B}), \tag{1}$$

where $\vec{m}$ is the magnetization of the bead in the external magnetic field $\vec{B}$ (7). However, practical use of this relationship may be limited due to complexity in the field configuration or variability in bead size and magnetization density.

An alternate approach to force calibration is to employ measurements of the Brownian motion of the bead itself: the variance of the bead motion in x and y is inversely related to the applied force (3,7). Depending on the type of instrumentation employed in the magnetic tweezers, however, this approach has limitations. In particular, the movements of the bead in x and y are typically recorded with a charge-coupled device (CCD) camera. However, finite camera acquisition frequencies may introduce artifacts in variance measurements due to camera blurring and aliasing, as has been noted elsewhere (19–21). This may lead to systematic biases, particularly for short constructs such as nucleic acid hairpins (22) in which

Submitted April 22, 2010, and accepted for publication June 3, 2010.

△Aartjan J. W. te Velthuis and Jacob W. J. Kerssemakers contributed equally to this work.

*Correspondence: n.h.dekker@tudelft.nl

Editor: Laura Finzi.

0006-3495/10/08/1292/11 $2.00

doi: 10.1016/j.bpj.2010.06.008

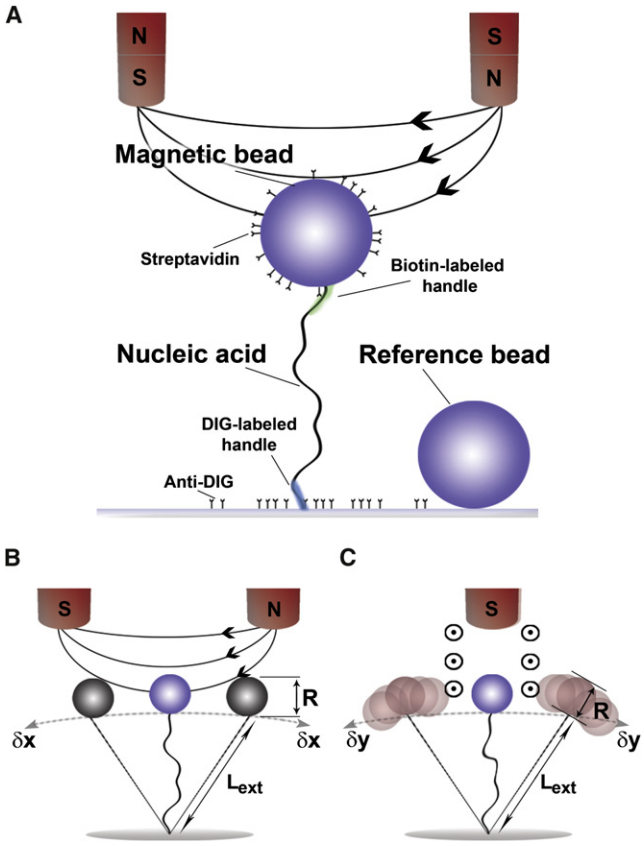

FIGURE 1 Motion of a tethered particle. (*A*) In a magnetic-tweezers setup, a nucleic acid polymer is tethered by digoxigenin and biotin-labeled handles between an antibody-coated surface and a streptavidin-coated paramagnetic bead. A nonmagnetic bead attached to the surface functions as reference bead during particle tracking in x, y, and z to subtract low-frequency mechanical drifts from the microscope. (*B*) An illustration of the motions of a tethered bead in x with the magnetic field lines (*black lines*) pointing predominantly in the x direction. The magnetization consequently forces the bead to maintain alignment with the field. Such an alignment with the magnetic field only takes place at large enough forces, as discussed elsewhere (30). (*C*) A schematic of the motions of the tethered bead in y with the field lines (*black circles*) oriented predominantly perpendicular to the y direction. In this direction, the beads are able to freely rotate.

the tethered bead-nucleic acid system's response time (inversely proportional to the system's natural frequency) approaches or is shorter than the time the camera shutter is open. Corrections for these deleterious effects of camera blurring and aliasing can be implemented by examining the bead's fluctuations in the spectral domain (19).

In theory the approach to accurately measure the bead variance by correction for systematic acquisition biases can be expected to work successfully up until the point where the natural frequency of the system approaches the Nyquist frequency of the camera (f_{Nyq}, equal to one-half of the sampling frequency) (19,23). However, the limitations of this approach have not been systematically explored for MT experiments, and it is presently undocumented within which force regime this approach can be reliably applied. A tool to quantitatively explore the correction limits, chart the effects of MT setup parameters, and define where tradeoffs appear between the magnitude of the calibration error and the height of the applied force, is thus desirable. This would allow users to make the biases of the system explicit and then optimize conditions for a given application without the need to extensively test configurations. Those experiments in which the use of small beads is required to minimize low frequency noise or in which high forces need to be applied to unwind double-stranded regions in the template (i.e., >14 pN) would highly benefit from such carefully investigated guidelines (22,24,25).

Here, we have systematically evaluated the limitations of MT spectral analysis and the efficacy of camera correction. To do so, we have developed an MT simulator that simulates the Brownian dynamics (26) of a tethered bead molecule in three dimensions, generating $x(t)$, $y(t)$, and $z(t)$ traces as a function of user-defined parameters. An emulated camera then simulates the sampling effects that are commonly encountered in real-time measurements, such as blurring and aliasing. Analysis of the simulated camera output demonstrates that it is in quantitative agreement with experimental data taken for tethered constructs under known magnetic forces. When deconvolution of the modified spectrum is used to recover the correct signal at a defined pulling force, our analysis reveals that accurate measurements (<10% error) can be conducted in the absence of camera aliasing and blurring correction until the natural frequency of the tethered bead system reaches ~50% of f_{Nyq}. This limit is raised to ~80% when spectral corrections are applied, although higher forces can be measured when the error constraint is relaxed. As the natural frequencies in MT are directly related to bead size, contour length, and sample viscosity, higher forces can alternatively be measured by optimizing these parameters for a given MT setup. By systematically varying these parameters, we explored the upper limits of force measurements with <10% error. Overall, our analysis gives insight into the systematic biases in MT experiments and provides general guidelines that can be used to correctly design MT experiments.

THEORETICAL BACKGROUND

In an MT, a magnetic force (F_{mag}) is applied on a nucleic acid or protein tether in the z direction. This force is effectively constant over the range of motion explored by the tether. F_{mag} is counteracted by the restoring force originating from the tether, which gives the total potential energy of the system,

$$E_p = E_{\mathrm{tether}} + E_{\mathrm{magnet}} = A(L_{\mathrm{ext}}) - F_{\mathrm{mag}} \cdot z, \qquad (2)$$

where $A(L_{\mathrm{ext}})$ is the energy stored in the nucleic acid as function of the extension of the tether L_{ext}. In equilibrium,

all partial derivatives must be equal to zero and we can thus write

$$(x, y, z) = (0, 0, L_{\text{ext}}) = \vec{r}_0.$$

From this first-order condition, it follows that

$$F_{\text{mag}} = \frac{\partial \text{A}}{\partial L_{\text{ext}}}. \tag{3}$$

The tethered bead system is constantly forced out of this equilibrium by Brownian motion, which creates movements both in the direction of the field (which we take to be the x direction) and perpendicular to the field (which we define as the y direction). Note that in the x direction, the orientation of the magnetic bead is constrained by its alignment with the magnetic field, thus preventing rotation about its axis (Fig. 1 *B*). In the y direction, conversely, the orientation of the bead is unconstrained, and thus the bead will align itself with the nucleic acid tether, making L_{ext} appear longer by an amount equal to the radius of the bead (Fig. 1 *C*). When we evaluate the second partial derivatives, the total potential energy around the equilibrium position is given to second order by (27)

$$\begin{aligned} E_{\text{p}}(\vec{\mathbf{r}}) &\approx E_{\text{p}}(\vec{\mathbf{r}}_0) + \frac{1}{2}k_x\delta x^2 + \frac{1}{2}k_y\delta y^2 + \frac{1}{2}k_z\delta z^2 \\ E_{\text{p}}(\vec{\mathbf{r}}) &\approx E_{\text{p}}(\vec{\mathbf{r}}_0) + \frac{1}{2}\left(\frac{F}{L_{\text{ext}}}\right)\delta x^2 + \frac{1}{2}\left(\frac{F}{L_{\text{ext}} + R}\right)\delta y^2 \\ &\quad + \frac{1}{2}\left(\frac{\partial F}{\partial L_{ext}}\right)\delta z^2, \end{aligned} \tag{4}$$

where R is the bead radius, and k_x, k_y, and k_z are the trap stiffness in x, y, and z, respectively. In the z direction, the motions of the bead are dependent on the local variation of the restoring force, which can be calculated from models of polymer elasticity. For a double-stranded nucleic acid tether, we here use the z derivative of the inextensible wormlike chain (WLC) model as an approximation for the spring constant k_z. The three stiffnesses in the MT are

$$k_x = \frac{F}{L_{\text{ext}}}, \tag{5}$$

$$k_y = \frac{F}{L_{\text{ext}} + R}, \tag{6}$$

$$k_z = \frac{\partial F(L_{\text{ext}})}{\partial L_{\text{ext}}} = \frac{k_{\text{B}}T}{2L_pL_0}\cdot\left(2 + \left(1 - \frac{L_{\text{ext}}}{L_0}\right)^{-3}\right), \tag{7}$$

where L_p is the persistence length, L_0 the contour length of the nucleic acid tether, k_{B} the Boltzmann constant, and T the absolute temperature. Note that for simulations of different tethers, e.g., consisting of ssDNA or protein, other spring constants for the z direction may need to be used. With $\langle\delta x^2\rangle$, the variance of the bead excursions in the x direction, the equipartition theorem directly provides an estimation of the force, as described previously (3):

$$F = \frac{k_{\text{B}}TL_{\text{ext}}}{\langle\delta x^2\rangle}. \tag{8}$$

EXPERIMENTAL PARAMETERS

Experimental configuration of magnetic tweezers

We use an MT setup similar to that developed and described by Strick et al. (3) (Fig. 1) as published elsewhere (28). Briefly, a CCD camera with a sampling frequency of 120 Hz (TM-6710CL, PULNix America, JAI, Sunnyvale, CA) was used to track superparamagnetic beads of 2.8 μm in diameter (M-280 beads; Life Science Products, Frederick, CO) tethered to the surface. As magnets, we used gold-plated (Ni-Cu-Ni-Au), 5 × 5 × 5 mm neodymium-iron-boron permanent magnets (SuperMagnete, Uster, Switzerland). As tether, we used a 7.9- or 3.6-kb dsDNA construct with multiple biotin and digoxigenin labels at the ends (29). Flow cells were made from microscope coverslips with parafilm spacers. Surfaces were passivated with bovine serum albumin (10 mg/mL), while measurements were performed in phosphate buffered saline at room temperature. Reference beads were attached to the surface and imaged simultaneously with measurement beads to correct for mechanical drift. Bead fluctuations were tracked with an accuracy of ~5 nm.

Simulation of magnetic tweezers data

The simulation of the tethered beads and spectral analysis was performed in LabVIEW 8.6 (National Instruments, Austin, TX; source code is provided in the Supporting Material). Typical parameter values are listed in Table S1 in the Supporting Material, unless indicated otherwise for specific simulations.

RESULTS AND DISCUSSION

In an MT experiment, a DNA or RNA construct tethers a bead to a flow cell surface (Fig. 1 *A*). Due to Brownian motion, this bead is displaced from its equilibrium position, but constrained by both the applied force (governed by the bead's internal magnetization and the magnetic field) and the flexibility of the nucleic acid tether (Fig. 1, *B* and *C*). The Brownian motion of the bead in x is inversely related to the applied force and may thus be used to determine the force imposed onto the system (Eq. 8). MT experimental data, however, is typically obtained via image acquisition through a CCD camera, which may result in erroneous measurement of the force when tracking high-frequency Brownian movements.

To study the adverse effects of image acquisition on force measurements and determine how well they can be

corrected for, we have developed an MT simulator to which the effects of the camera can be applied. This simulated data was then compared to experimental traces of uncorrected MT data (see Magnetic Tweezers Simulations, below). We subsequently examined how well camera effects due to finite camera acquisition frequencies can be deconvoluted, and the extent to which this procedure limits the force calibration of MT experiments (see Approach to Correct for Camera Blurring and Aliasing, below). Furthermore, we investigated the effects of experimental conditions and how their optimization could improve the force calibration, and present these findings as general guidelines for the spectral analysis of MT data (see Guidelines to Spectral Analysis, below).

Magnetic tweezers simulations

Equation of motion of the tethered bead

To simulate a tethered bead system, we start with the Einstein-Ornstein-Uhlenbeck theory of Brownian motion (26), which defines a bead's movements in a harmonic trap with the associated Langevin equation,

$$m\cdot\ddot{x}(t) + \gamma\cdot\dot{x}(t) + k\cdot x(t) = F_{\text{therm}}, \tag{9}$$

where $x(t)$ is the position of the particle as function of time, m the inertial mass, k the trap stiffness, F_{therm} the thermal force on the particle by random collisions with water molecules, and γ the friction coefficient, which is itself defined as $\gamma = 6\pi\eta R = k_{\text{B}}T/D$, with D representing the bead's diffusion constant, and η the dynamic viscosity. Because the loss of kinetic energy through friction takes place over a very short time interval, $t_{\text{inert}} \equiv m/\gamma$ ($\sim 10^{-6}$ s), the inertial term is negligible. Defining ω as the frequency in radians per second, the theoretical power spectrum $P(\omega)$ of the Brownian fluctuations is given by (19)

$$P(\omega) \equiv \left|x^2(\omega)\right| = \frac{2\gamma k_{\text{B}}T}{\gamma^2\omega^2 + k^2}, \tag{10}$$

whose integral can be fit with an arctangent. The radial cutoff frequency of the system ω_c is defined as the frequency at which $P(\omega)$ is one-half its maximal value:

$$\omega_c = \frac{k}{\gamma} = \frac{kD}{k_{\text{B}}T}. \tag{11}$$

We will also frequently refer to the cutoff frequency in Hz, defined as $f_c = \omega_c/2\pi$, as this better facilitates comparison with experimental and simulated data. We note that γ is influenced by R, as discussed in the Supporting Material, and that an increase of the effective R near surfaces lowers the cutoff frequency of the system. Additionally, we note that at low forces the motion of the bead may change to coupled translation-rotations due to interactions with the surface (30). Because we focus our study on high forces, these effects have been omitted for simplicity.

For our simulation of motion in the MT, we assume that the motion of a tethered bead is induced by Langevin-force impulses of duration Δt, whose effective displacement ($\delta x_{\text{Langevin}}$) is drawn from a Gaussian distribution with $\langle\delta x\rangle = 0$ and $\langle\delta x^2\rangle = 2D\Delta t$ as detailed elsewhere for tethered particle motion (31,32). We can thus write for Δx:

$$\Delta x = \frac{-k_x x D}{k_{\text{B}}T}\Delta t + \delta x_{\text{Langevin}}(\Delta t). \tag{12}$$

Using Eqs. 5–7, we can write three equations of motion in MT:

$$\Delta x(t) = \frac{F}{L_{\text{ext}}}\cdot\frac{-xD}{k_{\text{B}}T}\Delta t + \delta x_{\text{Langevin}}(\Delta t), \tag{13}$$

$$\Delta y(t) = \frac{F}{L_{\text{ext}} + R}\cdot\frac{-yD}{k_{\text{B}}T}\Delta t + \delta x_{\text{Langevin}}(t), \tag{14}$$

$$\Delta z(t) = \frac{k_{\text{B}}T}{2L_pL_0}\cdot\left(2 + \left(1 - \frac{L_{\text{ext}}}{L_0}\right)^{-3}\right)\cdot\frac{-zD}{k_{\text{B}}T}\Delta t + \delta x_{\text{Langevin}}(\Delta t). \tag{15}$$

These equations allowed us to simulate a series of tethered bead excursions in x, y, and z directions, at user-defined forces and tether parameters (Fig. 2). We typically simulated traces with a time step Δt of 0.005 ms, which is small enough to correctly simulate the Brownian motion under high forces (Fig. S1, *A* and *C*). Shortening Δt did not significantly affect the outcomes of the spectral analysis.

The simulated variances are in agreement with experimental data

To obtain simulated data that was comparable to the experimental data derived from video microscopy, we emulated the effects of image acquisition by a CCD camera. In general, a camera samples at a finite camera or acquisition frequency f_s and integrates each sample point over a finite integration time or shutter time W, leading to motion blur and aliasing (see Approach to Correct for Camera Blurring and Aliasing, below, for details). To emulate the effects introduced by the CCD camera, we sampled the $x(t)$, $y(t)$, and $z(t)$ data at a fixed f_s and time-averaged each sample over a rectangular window of width W. For simplicity, we assume that f_s and the shutter frequency f_e ($f_e = 1/W$) are equal, i.e., $f_e = f_s$ (see Table S1). To ensure that the observed differences between the original and camera-averaged variances did not derive from a statistical error ε of force measurement at low forces, we used sufficiently long traces for our analysis (see Fig. S1 *B* and the Supporting Material). As shown in Fig. 3, camera averaging resulted in a reduction of the measured variance $\text{var}(x_m)$ of the bead's position compared to the true variance $\text{var}(x)$: $\text{var}(x_m) \leq \text{var}(x)$.

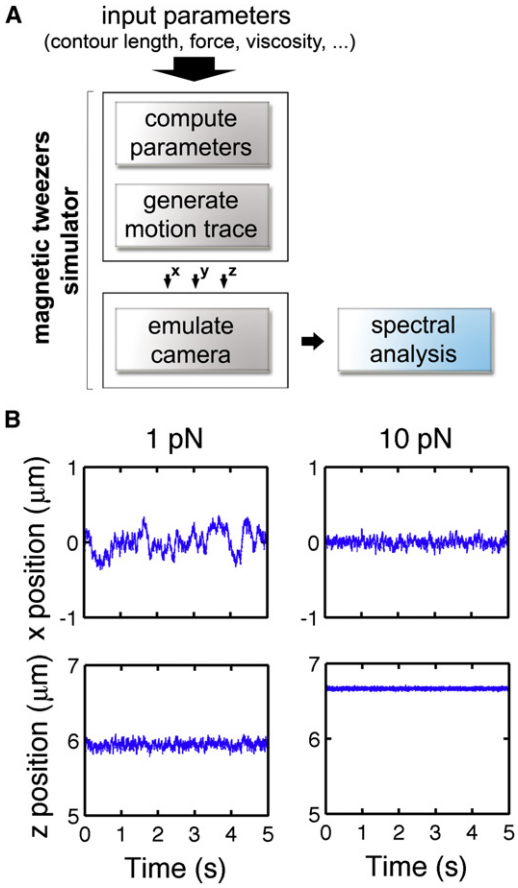

FIGURE 2 Simulation of a tethered particle. (*A*) Schematic presentation of simulation and analysis procedure, showing that the magnetic tweezers simulator consists of three modules: 1), parameter computation, 2), motion simulation, and 3), camera emulation. (*B*) Simulated traces of Brownian motion of a tethered bead in three dimensions. The input parameters for these simulations were 1.4 μm for the bead radius (R), 7 μm for the contour length (L_0), 50 nm for the persistence length (L_p), and either a 1 or 10 pN force applied in z. Changing the applied force readily results in different amplitudes in all three dimensions and a shift of the bead position in z.

To verify that the time-averaging was implemented correctly in the simulations, we compared time-averaged data from simulations and experiments by plotting 1), the simulated, time-averaged variances against the simulated force (F_{sim}); and 2), the experimentally measured variances against the magnetic force (F_{mag}). It should be noted that the latter is only possible when the calculated F_{mag} (computed using Eq. 1) is known to be an accurate measure of the force that was applied experimentally, as described previously for uniform beads in combination with the field configuration specified in Fig. 1 (7). As shown in Fig. 4, we find excellent agreement between the simulated bead variances (Fig. 4 *A*, *black squares*) and the experimental data (Fig. 4 *A*, *red circles*). The force-extension behavior of the simulated tethers (Fig. 4 *B*, *black squares*) also agrees well with the experimentally obtained data (Fig. 4 *B*, *red circles*) within the entropic regime of the inextensible WLC model (<10 pN), as expected.

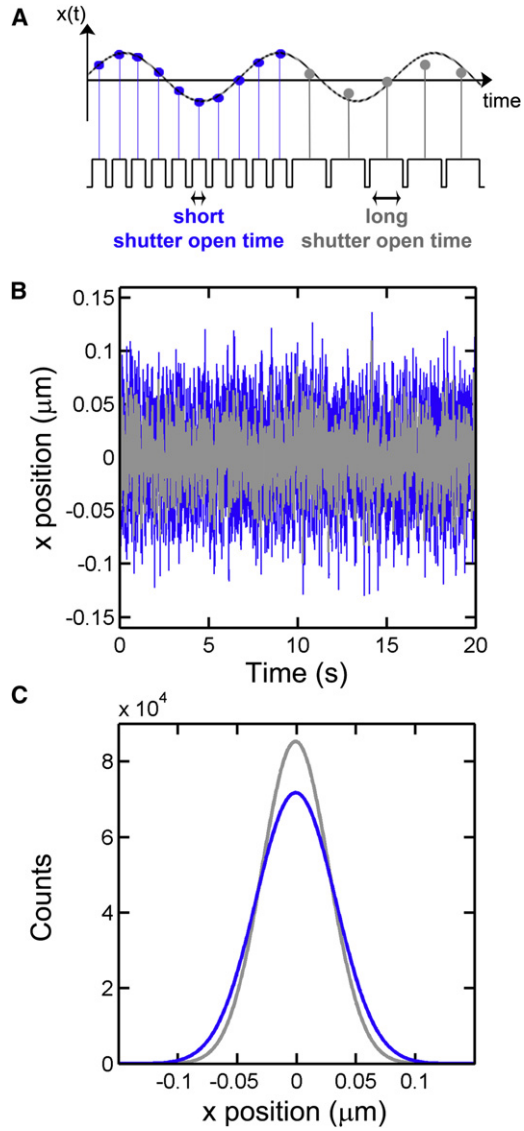

FIGURE 3 Effect of camera integration time on measurement of tethered bead fluctuations. (*A*) Illustration of the effect of camera sampling. Lower sampling frequencies combined with long shutter times result in averaging effects, thereby reducing the observed bead movements (*light gray*) relative to the true movements. (*B*) Simulated trace of a bead's position in x as function of time at 10 pN stretching force (*blue trace*). Sampling this simulated trace with an emulated camera with f_s of 120 Hz and shutter time of 8.3 ms clearly reduces the variance in x (*light gray trace*). (*C*) This effect is also evident when the variance in x is analyzed with a Gaussian fit to the histograms of the bead traces (same color-coding as in panel *B*). The simulations shown in this figure were performed as defined in Table S1, using a constant force of 10 pN.

Approach to correct for camera blurring and aliasing

Method to correct for the camera effects on measured spectra

According to the Nyquist theorem, camera sampling with a finite f_s can bring about significant errors when tracking

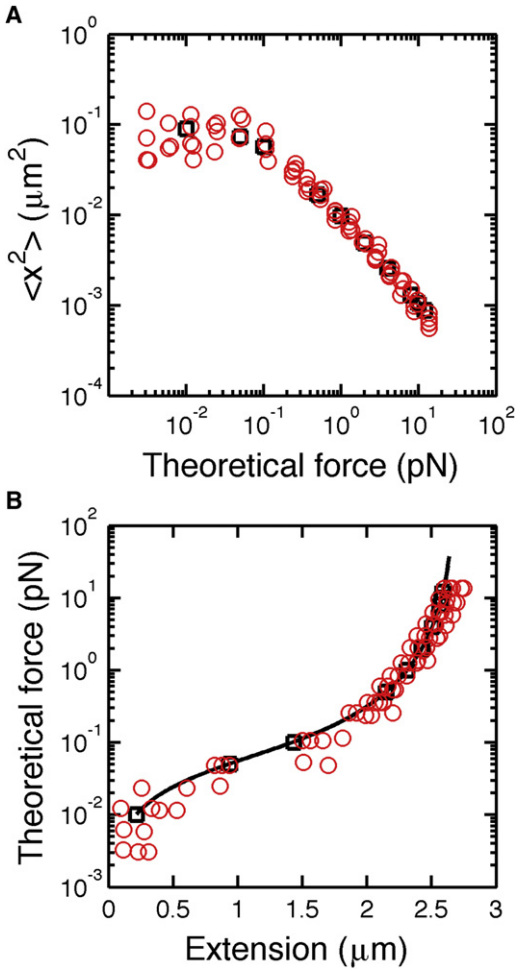

FIGURE 4 Verification of simulator output with experimental data. (*A*) The output of the simulations was tested by 1), plotting the simulated mean variance in x as function of F_{sim} (*squares*) and 2), comparing it to the experimentally obtained variances for DNA-tethered beads against the applied F_{mag} (*circles*). The latter force was computed from beads confirmed to have uniform magnetization as described elsewhere (7). Note that, to clearly distinguish the forces computed here from those forces deduced via analysis of the bead fluctuations (see Eq. 8), we have labeled them in this figure as "theoretical force". (*B*) The output of the simulation was also tested by plotting the simulated extensions (*squares*) and experimental extension (*circles*) against the theoretical force (see note in panel *A*). Both agree well within the entropic regime of the inextensible WLC (<10 pN), as expected. The fit parameters for the inextensible wormlike chain model are $L_0 = 2.7$ μm and $L_p = 51$ nm.

frequencies higher than half f_s. In general, sampling Brownian motion with a camera results in two effects. The first is time-averaging or motion blur, and leads to var(x_m) being lower than var(x), as mentioned above (Fig. 3 *B*). The second is aliasing, which results in a contribution to the frequencies of the measured spectrum by signal components that are higher than f_s. This principle is also known as back-folding, and although it does not affect the power of the spectrum, it does change its shape, and consequently the cutoff frequency of the system.

If we assume that the integration window of the camera is rectangular (Fig. 3 *A*), we define $P_{\text{window}}(\omega)$, the power spectrum of the moving average window, by

$$P_{\text{window}}(\omega) = \left(\frac{\sin(\omega W/2)}{\omega W/2}\right)^2. \quad (16)$$

To retrieve the underlying, correct variance from the incorrect, measured var(x_m), we start with the measured power spectrum P_m, iteratively correct it (see Eqs. 17–19 below), and fit the integral of the spectrum with an arctangent until the fitting error reaches a value below 10^{-4} μm^2/Hz.

The correction steps we include are the following:

First, we account for the finite exposure effect of the camera, which increases the power in the higher frequencies that was lost by camera-based sampling (in Fig. 5, compare

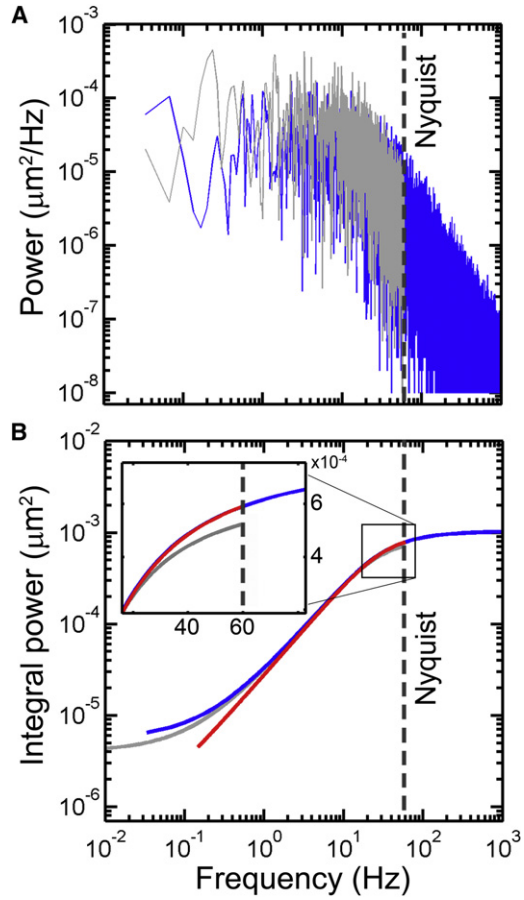

FIGURE 5 Means of correcting the camera-sampled fluctuations. (*A*) Simulation of the power spectral density of the bead fluctuations in $x(t)$ (*blue points*, without camera emulation; *gray points*, with camera emulation) results in a loss of signal beyond f_{Nyq} (here 60 Hz) and averaging effects over the measured frequencies. (*B*) The integrated spectra can be fit to an arctangent to yield the variance in x. (*Inset*) The integral to the corrected power spectrum (*red*) produces the same result as the fit to the integral of the original power spectrum (*blue*), but the fit to the integral of the camera-sampled spectrum (*gray*) clearly differs from the fit to the integral of the original power spectrum.

original *blue spectrum* to sampled *gray spectrum*, and the sampled spectrum to the corrected *red spectrum*) by dividing the measured spectrum P_m through the blur correction term C_{blur} (19):

$$C_{\text{blur}}(\omega) = \left(\frac{\sin(\omega W/2)}{\omega W/2}\right)^2. \quad (17)$$

Second, we account for potentially back-folded frequency components from the measured spectrum with the alias correction term C_{alias}, which is subtracted from the measured spectrum (see Eq. 19 below). Although in principle this correction has to be performed for an infinite number of terms, the first two antialiasing terms (i.e., $n = -1$ and $n = 1$) provide sufficient estimation of the alias effects of the camera given the rapid decay in contribution of higher order terms. Indeed we find that based on the data presented in Fig. 6, the effect of accounting for the first two terms is ~30% and ~1%, respectively. We write for C_{alias} (19)

$$C_{\text{alias}}(\omega) = \sum_{n=-1,+1}\left[\frac{2\gamma k_B T}{\gamma^2(\omega + n\cdot\omega_s)^2 + k^2}\right]\cdot\left(\frac{(\sin(\omega + n\cdot\omega_s)W/2)}{(\omega + n\cdot\omega_s)W/2}\right)^2, \quad (18)$$

where ω_s is the radial sampling frequency ($\omega_s = 2\pi f_s$). Additionally, each antialiasing term is itself corrected for blurring through multiplication by a C_{blur} term. Using Eqs. 17 and 18, we can now correct the measured power spectrum and obtain a correctly fitted var(x) after integration of the spectrum (Fig. 5 *C*), using

$$P_{\text{corrected}}(\omega) = \frac{P_m - C_{\text{alias}}}{C_{\text{blur}}}. \quad (19)$$

Performance of camera correction terms in MT simulations

Having validated the MT simulator, we now have a tool to explore the effect of the various steps in the correction procedure on computing var(x) from var(x_m). In particular, we will systematically apply either no correction and account for blur effects only by iteratively dividing P_m through Eq. 17, or else account for both blur and antialiasing by using Eq. 19 and plot the forces and cutoff frequencies obtained through spectral analysis against the theoretical F and f_c that were used as inputs in the simulation. Ideally, the theoretical force and cutoff frequencies should be equal to the values obtained from the analysis. As an additional test for the correction efficiency, we will also derive R from the spectral analysis, which follows directly from f_c via $f_c = k/(12\pi^2\eta R)$ (see Eq. 11). This R should be constant and equal to the bead radius that we define in our simulation. In experimental situations, the measured R also presents a simple confidence measure, provided that the true bead radius is known (e.g., provided by the manufacturer).

When we apply no correction to the recorded spectrum, we observe an overestimation of the force due to averaging effects of the camera. Specifically, an error of 10% is reached at forces of 14 pN for a 2.7-μm dsDNA construct, and this error becomes larger when more force is applied (Fig. 6 *A*, *red squares*). At these forces, the natural frequency of the system exceeds 32 Hz, or approximately one-fourth of f_s (Fig. 6 *B*). If we apply the blur correction only, we observe a systematic underestimation of the force when $F > 14$ pN (Fig. 6, *A* and *B*, *black triangles*). We thus find that applying solely a blur correction to the recorded spectrum does not provide a more reliable calibration of the force than spectral analysis without blur correction. However, if we apply the aliasing correction only (i.e., no blur correction), we find already a >10% overestimation of the force at 1 pN (data not shown).

Fortunately, when we subsequently account for both blur and the $n = -1$ term of the antialias (Eq. 18), a significant reduction in the error is observed, which thus facilitates calibration of higher forces with the same confidence (Fig. 6 *A*, *green triangles*). This effect is apparent in both the correction of the force (Fig. 6 *A*) and the estimation of R, our additional control (Fig. 6 *C*). In fact, we can observe in Fig. 6, *B* and *C*, that if both blur and aliasing corrections are taken into account, reliable measurements of the mean applied force can be performed for cutoff frequencies much closer to f_{Nyq} or even beyond f_{Nyq}. When we specifically look at the mean force obtained within <10% error and small standard deviations, we see that we can correctly measure forces up to ~19 pN, or $f_c \sim 46$ Hz. Finally, when we account for the $n = 1$ term in the antialias as well, we observe a small additional increase (~1%) in force-measurement confidence (Fig. 6 *A*, *blue circles*), which is in accordance with the rapid decay in contribution of the alias terms. Overall, we demonstrate that when all camera correction terms are applied, force measurements can be accurately performed within 10% error for tethered bead systems with cutoff frequencies <47 ± 2 Hz (e.g., 20 ± 1 pN for a 2.7-μm DNA tether). This is close to 80% of f_{Nyq}.

Correction of experimental data

Having explored the spectral correction procedure on simulated data, we next apply this procedure to experimental MT traces. To this end, we obtained experimental data for two relatively short DNA construct lengths—namely, 7.9 kb (~2.7 μm) and 3.6 kb (~1.2 μm). We subsequently analyzed

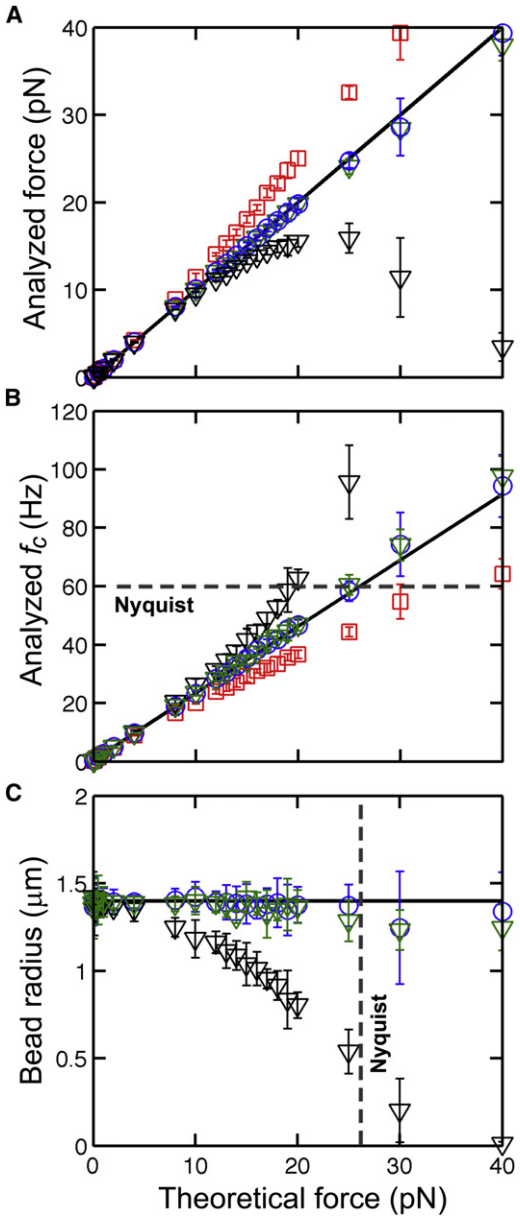

FIGURE 6 Effectiveness of spectral corrections of the fluctuations. (*A*) Simulated force, and the force deduced from the transverse fluctuations through spectral analysis. (*B*) Simulated force and the cutoff frequency (f_c) derived from spectral analysis. (*C*) Deduction of R via spectral analysis of the fluctuations, plotted as function of the force. The deviation between the measured R as obtained after spectral analysis and the expected value for R can be used a measure for the extent to which the spectral analysis yields correct values for the forces. In panels *A–C*, the following coding is employed: input parameters (*black line*), analysis in the absence of any correction for camera sampling (*squares*), analysis with blur correction (*black triangles*), analysis with blur and the $n = -1$ alias correction (*green triangles*), and analysis including the complete correction including blur, alias $n = 1$, and alias $n = -1$ corrections (*circles*). We find that the alias $n = 1$, and alias $n = -1$ corrections contribute 30% and 1% to the correction, respectively. Error bars represent standard deviation of five complete repeats of data simulation and analysis.

$x(t)$ data acquired with these molecules and corrected P_m for both blur and aliasing effects. As we already confirmed that our MT simulator was able to correctly reproduce the relation among the force, extension, and Brownian motion of a tethered magnetic bead within the entropic regime of the WLC (Fig. 4), we simulated data sets specific for the experimental configurations used and were thus able to assess the efficacy of the spectral analysis of experimental data through direct comparison.

For the 7.9-kb dsDNA construct, we observe good agreement between the simulated and experimental data sets at forces <10 pN (Fig. 7 *A*, compare *red circles* and *black squares*). We also observe that R obtained from the analysis of the experimental data was within the expected error (Fig. S4). At forces >10 pN, deviations can be observed between the experimental and simulated force-extension data (Fig. 7 *A*, compare *blue circles* and *black squares*). This is, however, in accordance with the inextensible WLC fit model used for the simulation as demonstrated by the fit to the experimental data (Fig. 7 *A*, *black line*). When we analyze the data for the 3.6-kb construct, we find that deviations between the simulated and experimental data already start to occur at ~3 pN (Fig. 7 *B*, compare *squares* with *circles*). At this force, f_c exceeds 47 Hz. As established using the MT simulator, this f_c corresponds to the 10% error threshold that is reached by the spectral analysis, thus explaining the deviation. Additionally, we also observe that at higher forces (i.e., >3 pN), significant deviations become apparent between the bead radius obtained via spectral analysis and the original R (not shown). The 7.9-kb tether remained well below this threshold over the entire force range used (Fig. S2). This thus demonstrates that we can correctly measure forces in experimental MT setups, but that we have to be aware of the limitations of the spectral analysis, as identified using the MT simulator. Additionally, these results reveal that one should be able to measure higher forces with higher confidence when the L_0 of the tether increases, and, consequently, k_x and f_c decrease.

Guidelines to spectral analysis

Validation of the correction procedure with experimental data puts us in a position to explore the limits of our approach and to provide guidelines for optimizing tethered bead calibrations. This is particularly vital when relatively high forces have to be measured with good accuracy (e.g., errors <10%). When short tethers are not essential for the experiment, a long L_0 will generally provide good results, as shown in Fig. 8 *A*. In this plot, the 10% error limit is presented as a function of L_0. We readily see that when $L_0 > 2$ μm and $R = 1.4$ μm, forces of 10 pN can be reliably measured with 10% accuracy without camera correction procedures (Fig. 8, *black circles*). We can also observe in Fig. 8 that the 10% limit rises linearly with L_0.

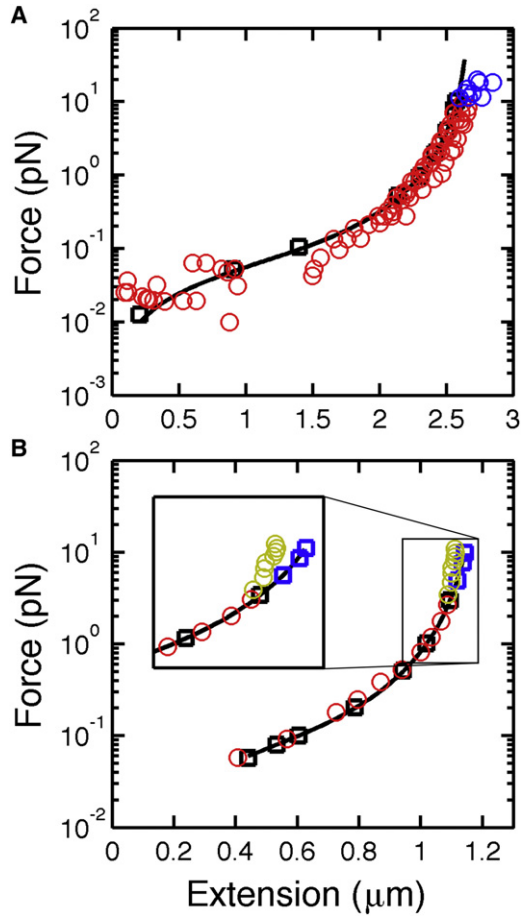

FIGURE 7 Application of spectral corrections to experimental data. (*A*) Force extension curve obtained after spectral analysis of tethered bead simulations (*squares*) or experimental data (*circles*) for a dsDNA molecule with a contour length of 2.7 μm (~7.9 kbp). Also shown is the fit of the inextensible wormlike chain model (fit parameters are $L_0 = 2.7$ μm and $L_p = 49$ nm). (*Blue circles*) Data points beyond the applicable range of the inextensible WLC model. Note that the natural frequency did not exceed 47 Hz (see Fig. S2). (*B*) Force extension curve obtained after spectral analysis of tethered bead simulations (*squares*) or experimental data (*circles*) of a dsDNA molecule with an L_0 of 1.2 μm (~3.6 kbp) show good agreement at cutoff frequencies <47 Hz (~3 pN). At higher forces, the points between the simulated data, the fit to inextensible WLC model (*black line*; parameters are $L_0 = 1.2$ μm and $L_p = 45$ nm) and experimental data start to diverge (indicated with different colors). Both simulated and experimental data were corrected for blurring and aliasing effects.

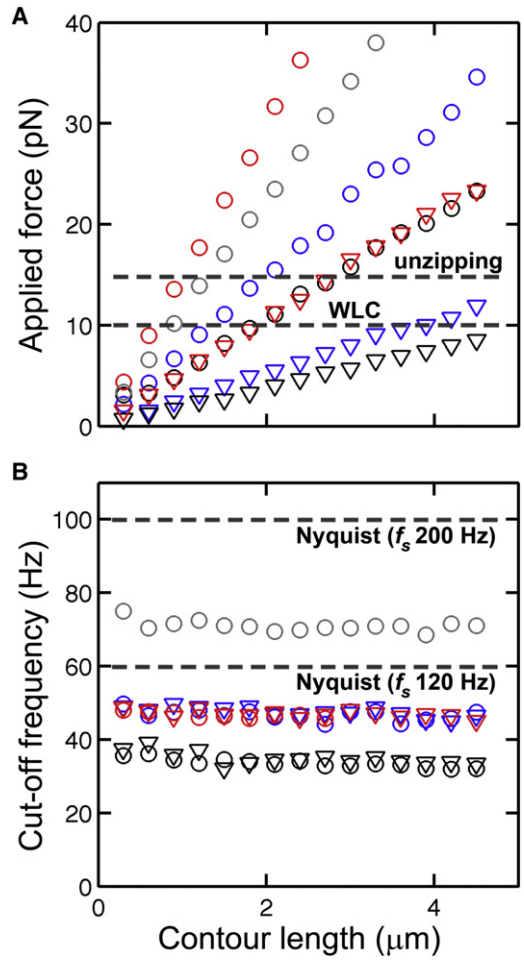

FIGURE 8 Force measurements at a 10% error limit using various experimental parameters. (*A*) DNA constructs tethered to beads with a radius of 1.4 μm (*circles*) or a radius of 0.5 μm (*triangles*) were used to create 10% error plots under varying conditions. Curves are shown for uncorrected spectral analysis (*black*), camera-corrected analysis (*blue*), camera-corrected analysis for traces simulated at a twofold higher viscosity (*red*), and camera-corrected analysis for traces sampled at 200 Hz instead of 120 Hz (*gray*). (*Dotted lines*) Range of validity of the inextensible WLC model (<10 pN) and the unzipping force required to open a typical DNA hairpin. (*B*) The cutoff frequencies for the tethered bead systems simulated in panel *A*. This illustrates that applying spectral analysis corrections for blurring and aliasing allows one to measure, within 10% error for cutoff frequencies, close to 80% of f_{Nyq}.

When high forces have to be achieved for relatively short L_0, 1), the application of spectral corrections, 2), implementation of faster camera frequencies, 3), use of high viscosity buffers, or 4), introduction of larger beads, are all options to be considered.

As shown in Fig. 8 *A*, for the first alternative, when we initially apply both the blur and alias correction we can reliably measure forces (error < 10%) that are 1.4-fold higher compared to the situation in which camera corrections are not implemented (Fig. 8 *A*, compare *black* and *blue circles*). More specifically, we can now measure forces close to 8 pN with 1-μm tethers (~3 kb dsDNA, $R = 1.4$ μm). We find similar differences between uncorrected and corrected forces when beads are used with a 0.5-μm radius (Fig. 8 *A*, *triangles*).

For the second alternative, the accurate measurement of even higher forces can be achieved by increasing the sampling frequency of the camera (Fig. 8 *A*, *gray circles*). As an example, we emulated a sampling frequency of 200 Hz and observed that the 10% error limit was raised to ~12 pN for 1-μm tethers. This is an improvement of ~1.5-fold relative to the blur- and alias-corrected force measurements.

The third alternative to improve correct measurement of higher forces is by increasing the viscosity of the calibration buffer (Fig. 8 *A*, *red circles*). In general, the force that can be accurately measured increases linearly with increasing viscosity, e.g., doubling the viscosity raises the force limit by a factor of 2, thereby raising the 10% error limit to ~15 pN for 1-μm tethers. Such higher viscosities are relatively easy to achieve, as, e.g., 25% glycerol raises the viscosity by a factor of ~2 at room temperature. However, higher viscosities may not be suitable to all experiments as they may change enzyme behavior and complicate cross-comparisons with the literature. This may be solved by first performing a magnet-and-construct calibration at high viscosity, before the actual experiment is done in a low viscosity buffer after buffer exchange (33).

The fourth alternative is an increase of bead size. As an example, for the experiments here, we used beads with a radius of 1.4 or 0.5 μm for our force measurements and can readily see that increasing the bead radius gives a linear increase of the force limit for the same error magnitude (in Fig. 8 *A*, compare *triangles* and *circles*). The range of bead sizes is, of course, limited by what manufacturers can supply. Furthermore, the use of larger beads may be less desirable when short tethers are used, as this may change the geometry of the bead's behavior in the magnetic field (e.g., rolling along its attachment) and introduce interactions of the bead with the surface of the flow cell (30). Moreover, larger bead sizes are accompanied by poorer time resolution, as γ is directly related to R (see Magnetic Tweezers Simulations, above). The choice of R will thus be a trade-off between the force range and correct experimental design.

SUPPORTING MATERIAL

Twenty-one equations, two tables, and four figures are available at http://www.biophysj.org/biophysj/supplemental/S0006-3495(10)00718-6.

We thank Susanne Hage, Iwijn de Vlaminck, and Gary Skinner for assistance with DNA construction, helpful discussions, and providing experimental data.

This work was supported by the Netherlands Organization for Scientific Research via a Veni grant (to J.L.), Vidi grant (to N.H.D.), a Toptalent grant (to A.J.W.t.-V.), and the European Science Foundation via a European Young Investigators grant (to N.H.D.).

REFERENCES

1. Tinoco, Jr., I., P. T. Li, and C. Bustamante. 2006. Determination of thermodynamics and kinetics of RNA reactions by force. *Q. Rev. Biophys.* 39:325–360.
2. Neuman, K. C., and A. Nagy. 2008. Single-molecule force spectroscopy: optical tweezers, magnetic tweezers and atomic force microscopy. *Nat. Methods.* 5:491–505.
3. Strick, T. R., J. F. Allemand, …, V. Croquette. 1996. The elasticity of a single supercoiled DNA molecule. *Science.* 271:1835–1837.
4. Danilowicz, C., C. H. Lee, …, M. Prentiss. 2009. Single molecule detection of direct, homologous, DNA/DNA pairing. *Proc. Natl. Acad. Sci. USA.* 106:19824–19829.
5. Kruithof, M., F. T. Chien, …, J. van Noort. 2009. Single-molecule force spectroscopy reveals a highly compliant helical folding for the 30-nm chromatin fiber. *Nat. Struct. Mol. Biol.* 16:534–540.
6. Kruithof, M., F. Chien, …, J. van Noort. 2008. SubpicoNewton dynamic force spectroscopy using magnetic tweezers. *Biophys. J.* 94:2343–2348.
7. Lipfert, J., X. Hao, and N. H. Dekker. 2009. Quantitative modeling and optimization of magnetic tweezers. *Biophys. J.* 96:5040–5049.
8. Ribeck, N., and O. A. Saleh. 2008. Multiplexed single-molecule measurements with magnetic tweezers. *Rev. Sci. Instrum.* 79:094301.
9. Ajjan, R., B. C. Lim, …, R. A. Ariëns. 2008. Common variation in the C-terminal region of the fibrinogen β-chain: effects on fibrin structure, fibrinolysis and clot rigidity. *Blood.* 111:643–650.
10. Mierke, C. T., P. Kollmannsberger, …, W. H. Goldmann. 2008. Mechano-coupling and regulation of contractility by the vinculin tail domain. *Biophys. J.* 94:661–670.
11. Strick, T. R., V. Croquette, and D. Bensimon. 1998. Homologous pairing in stretched supercoiled DNA. *Proc. Natl. Acad. Sci. USA.* 95:10579–10583.
12. Celedon, A., I. M. Nodelman, …, S. X. Sun. 2009. Magnetic tweezers measurement of single molecule torque. *Nano Lett.* 9:1720–1725.
13. Abels, J. A., F. Moreno-Herrero, …, N. H. Dekker. 2005. Single-molecule measurements of the persistence length of double-stranded RNA. *Biophys. J.* 88:2737–2744.
14. Mosconi, F., J. F. Allemand, …, V. Croquette. 2009. Measurement of the torque on a single stretched and twisted DNA using magnetic tweezers. *Phys. Rev. Lett.* 102:078301.
15. Koster, D. A., K. Palle, …, N. H. Dekker. 2007. Antitumor drugs impede DNA uncoiling by topoisomerase I. *Nature.* 448:213–217.
16. Koster, D. A., V. Croquette, …, N. H. Dekker. 2005. Friction and torque govern the relaxation of DNA supercoils by eukaryotic topoisomerase IB. *Nature.* 434:671–674.
17. Leuba, S. H., M. A. Karymov, …, J. Zlatanova. 2003. Assembly of single chromatin fibers depends on the tension in the DNA molecule: magnetic tweezers study. *Proc. Natl. Acad. Sci. USA.* 100:495–500.
18. Neuman, K. C., G. Charvin, …, V. Croquette. 2009. Mechanisms of chiral discrimination by topoisomerase IV. *Proc. Natl. Acad. Sci. USA.* 106:6986–6991.
19. Wong, W. P., and K. Halvorsen. 2006. The effect of integration time on fluctuation measurements: calibrating an optical trap in the presence of motion blur. *Opt. Express.* 14:12517–12531.
20. Berg-Sørensen, K., and H. Flyvbjerg. 2004. Power spectrum analysis for optical tweezers. *Rev. Sci. Instrum.* 75:594–612.
21. Savin, T., and P. S. Doyle. 2005. Static and dynamic errors in particle tracking microrheology. *Biophys. J.* 88:623–638.
22. Lionnet, T., M. M. Spiering, …, V. Croquette. 2007. Real-time observation of bacteriophage T4 gp41 helicase reveals an unwinding mechanism. *Proc. Natl. Acad. Sci. USA.* 104:19790–19795.
23. Wong, W. P., and K. Halvorsen. 2009. Beyond the frame rate: measuring high-frequency fluctuations with light-intensity modulation. *Opt. Lett.* 34:277–279.
24. Kim, K., and O. A. Saleh. 2009. A high-resolution magnetic tweezer for single-molecule measurements. *Nucleic Acids Res.* 37:e136.
25. Storm, C., and P. C. Nelson. 2003. Theory of high-force DNA stretching and overstretching. *Phys. Rev. E.* 67:051906.
26. Ermak, D. L., and J. A. McCammon. 1978. Brownian dynamics with hydrodynamic interactions. *J. Chem. Phys.* 69:1352–1360.
27. Vilfan, I. D., J. Lipfert, …, N. H. Dekker. 2009. Magnetic tweezers for single-molecule experiments. *In* Handbook of Single-Molecule Biophysics. Springer, New York.

28. Lipfert, J., D. A. Koster, …, N. H. Dekker. 2009. Single-molecule magnetic tweezers studies of type IB topoisomerases. *Methods Mol. Biol.* 582:71–89.
29. Crut, A., P. A. Nair, …, N. H. Dekker. 2008. Dynamics of phosphodiester synthesis by DNA ligase. *Proc. Natl. Acad. Sci. USA.* 105: 6894–6899.
30. Wong, P. W. 2006. Exploring single-molecule interactions through 3D optical trapping and tracking: from thermal noise to protein refolding. PhD thesis. Harvard University, Cambridge, MA.
31. Beausang, J. F., C. Zurla, …, P. C. Nelson. 2007. Elementary simulation of tethered Brownian motion. *Am. J. Phys.* 75:520–523.
32. Han, L., B. Lui, …, R. Phillips. 2008. Calibration of Tethered Particle Motion Experiments. Springer, New York.
33. Strick, T. 1999. Mechanical supercoiling of DNA and its relaxation by topoisomerases. PhD thesis. University of Paris VI, Paris, France.
34. van der Horst, A., and N. R. Forde. 2010. Power spectral analysis for optical trap stiffness calibration from high-speed camera position detection with limited bandwidth. *Opt. Express.* 18:7670–7677.